



First Chiral Catalan Solid Based on Molybdenum Halide with Efficient Circularly Polarized Luminescence in the Deep-Red Region

Sehrish Gull⁺, Wenkai Zhao⁺, Zhaoyu Wang, Yunxin Zhang, Haolin Lu, Xinyi Niu, Tianjiao Qiao, Hebin Wang, Tianyin Shao, Wenting Liu, Bing Sun, Hao-Li Zhang, Yongsheng Chen, and Guankui Long*

Abstract: The design of novel chiral metal halides with exceptional chiroptical properties has attracted significant research attention due to their potential applications in chiral optoelectronics and spintronics. However, developing the deep-red circularly polarized luminescence (CPL) emitters is still challenging. In this work, we presented the first chiral molybdenum halide clusters by incorporating chiral methylbenzylammonium (*R/S*-MBA) for the design of (*R*-MBA)₂Mo₆Cl₁₄ and (*S*-MBA)₂Mo₆Cl₁₄ tetrakis hexahedra, which adopt the unique Catalan solid structure. These chiral tetrakis hexahedra exhibit 24 unique 3c-2e Mo—Mo—Cl bonds, which are scarcely reported. Notably, these (*R*-MBA)₂Mo₆Cl₁₄ and (*S*-MBA)₂Mo₆Cl₁₄ tetrakis hexahedra demonstrated pronounced circularly polarized luminescence in the deep-red region, accompanied by an extended emission lifetime of 114.14 μs at room temperature. Additionally, these chiral molybdenum halide tetrakis hexahedra are optically stable for 3 months. The four-state spin sublevel model was employed to investigate the emission mechanism and found that the temperature-dependent exciton dynamics lead to the dual-band emission of the designed chiral tetrakis hexahedra. Our study expands the family of lead-free chiral metal halides and develops a novel strategy to design a high-performance deep-red CPL emitter.

Introduction

Circularly polarized luminescence (CPL) has drawn considerable attention owing to its fascinating potential applications in numerous fields such as 3D optical imaging,^[1] information encryption,^[2,3] biological probes,^[4-7] switches,^[8,9] and circularly polarized light sources.^[10,11] Chiral metal halides are

regarded as an ideal platform as a potential CPL light source, which exhibits peculiar features, including circular dichroism (CD), circularly polarized luminescence, nonlinear chiroptical effects, chirality-induced spin selectivity, and chiral-phonon assisted spin-Seebeck effect, etc.^[12-16] Red light, as one of the primary components of the visible spectrum, can regulate all the visible signals by mixing it with green and blue. Moreover, red CPL emitters hold substantial applications in white light illumination and full-color displays, especially for biological sensing and imaging due to the deep penetration,^[17-20] and also in communication systems.^[21] However, designing chiral metal halides with deep-red CPL emission is quite challenging. Therefore, developing the novel chiral hybrid metal halides with deep-red CPL emission and high color purity is highly needed.


Moreover, to address the toxicity issues associated with the chiral lead halides, researchers have introduced different environment-friendly metals such as Mn,^[22,23] Cu,^[24] Sb,^[25] In,^[26] Rb,^[27] Pt,^[28] Ru,^[13] Ce,^[29] and Bi.^[30] This approach has opened new opportunities for combining the advanced properties of different metals with chirality. Molybdenum (Mo) belongs to the family of cost-effective transition metals and offers several unique features, including high melting point, enhanced modulus of elasticity, low coefficient of thermal expansion, and high biosafety.^[31-34] Most importantly, molybdenum halide possesses luminescence in the deep-red region^[35,36] which is a promising avenue for integrating Mo as the inorganic part into the chiral metal halides to achieve efficient CPL emission in the deep-red region. However, chiral molybdenum halide has not been reported up to today. Therefore, it is highly needed to construct the

[*] S. Gull⁺, W. Zhao⁺, Z. Wang, Y. Zhang, H. Lu, X. Niu, T. Qiao, H. Wang, T. Shao, W. Liu, Prof. G. Long
Frontiers Science Center for New Organic Matter, Tianjin Key Lab for Rare Earth Materials and Applications, Smart Sensing Interdisciplinary Science Center, Renewable Energy Conversion and Storage Center (RECAST), School of Materials Science and Engineering, National Institute for Advanced Materials, Nankai University, Tianjin 300350, China
E-mail: longgk09@nankai.edu.cn

Prof. B. Sun, Prof. H.-L. Zhang
State Key Laboratory of Applied Organic Chemistry (SKLAOC), Key Laboratory of Special Function Materials and Structure Design (MOE), College of Chemistry and Chemical Engineering, Lanzhou University, Lanzhou 730000, China

Y. Zhang, Prof. Y. Chen
State Key Laboratory and Institute of Element-Organic Chemistry, Frontiers Science Center for New Organic Matter, The Centre of Nanoscale Science and Technology and Key Laboratory of Functional Polymer Materials, Renewable Energy Conversion and Storage Center (RECAST), College of Chemistry, Nankai University, Tianjin 300071, China

[⁺] Both authors contributed equally to this work.

 Additional supporting information can be found online in the Supporting Information section

chiral molybdenum halide and systematically investigate its chiroptical properties.

In this work, we designed and constructed the first chiral $(R\text{-MBA})_2\text{Mo}_6\text{Cl}_{14}$ and $(S\text{-MBA})_2\text{Mo}_6\text{Cl}_{14}$ tetrakis hexahedra by introducing chiral methylbenzylammonium ($R/S\text{-MBA}$). The tetrakis hexahedron belongs to the family of Catalan solids, which are the duals of the Archimedean solids. These convex isohedral polyhedral features a single dihedral angle, apart from the regular polyhedral. Among the 13 distinct shapes of Catalan solids, our system falls into the tetrakis hexahedron category. Structurally, it resembles a cube augmented with square pyramids and consists of 24 faces, 36 edges, and 14 vertices, conforming to the most famous Euler's polyhedron formula.^[37–40] Notably, the chiral $(R\text{-MBA})_2\text{Mo}_6\text{Cl}_{14}$ and $(S\text{-MBA})_2\text{Mo}_6\text{Cl}_{14}$ tetrakis hexahedra exhibit exceptional optical properties, including luminescence in the deep-red region with emission peaks at 658 and 698 nm and an ultra-long lifetime of 114.14 μs at room temperature. Due to the successful chirality transfer from the chiral organic cations to the molybdenum halide cluster, circular dichroism (CD) and circularly polarized luminescence (CPL) in the deep-red region were achieved. Moreover, these chiral $(R\text{-MBA})_2\text{Mo}_6\text{Cl}_{14}$ and $(S\text{-MBA})_2\text{Mo}_6\text{Cl}_{14}$ tetrakis hexahedra demonstrate 3-month optical stability and an enhanced photoluminescence quantum yield (PLQY) of 7.58%, surpassing the previously reported achiral molybdenum compounds. Our findings introduce a new and unique member to the chiral metal halide family, the tetrakis hexahedron cluster, and propose a novel strategy to design the high-performance deep-red CPL emitter.

Results and Discussion

The $(R\text{-MBA})_2\text{Mo}_6\text{Cl}_{14}$ and $(S\text{-MBA})_2\text{Mo}_6\text{Cl}_{14}$ single crystals were synthesized using a solvothermal method, with the detailed synthetic procedure in the experimental section. Single-crystal X-ray diffraction (SCXRD) analysis confirmed that $(R\text{-MBA})_2\text{Mo}_6\text{Cl}_{14}$ and $(S\text{-MBA})_2\text{Mo}_6\text{Cl}_{14}$ adopt a monoclinic crystal system with the *Sohncke* space group $P2_1$. Figure 1a illustrates the previously reported chiral metal halide clusters and highlights the structural resemblance of our designed system to the tetrakis hexahedron among the Catalan solids.

The $(R\text{-MBA})_2\text{Mo}_6\text{Cl}_{14}$ and $(S\text{-MBA})_2\text{Mo}_6\text{Cl}_{14}$ tetrakis hexahedra exhibit a typical zero-dimensional (0D) geometry with isolated $\text{Mo}_6\text{Cl}_{14}^{2-}$ tetrakis hexahedron separated by the chiral cations (as shown in Figure 1b). Due to the enantiomeric nature, the lattice constants of $(R\text{-MBA})_2\text{Mo}_6\text{Cl}_{14}$ and $(S\text{-MBA})_2\text{Mo}_6\text{Cl}_{14}$ tetrakis hexahedra are almost the same (as summarized in Table S1). The $\text{Mo}_6\text{Cl}_{14}^{2-}$ tetrakis hexahedron can be regarded as a combination of Mo_6 octahedron and Cl_{14} tetrakis hexahedron, and the mirror-symmetric structures for the $R\text{-Mo}_6\text{Cl}_{10}$ and $S\text{-Mo}_6\text{Cl}_{10}$ tetrakis hexahedra are also shown in Figures S1 and S2. The powder X-ray diffraction (PXRD) patterns of $(R\text{-MBA})_2\text{Mo}_6\text{Cl}_{14}$ and $(S\text{-MBA})_2\text{Mo}_6\text{Cl}_{14}$ tetrakis hexahedra exhibit sharp peaks with a slight shift from the simulated XRD, which is attributed

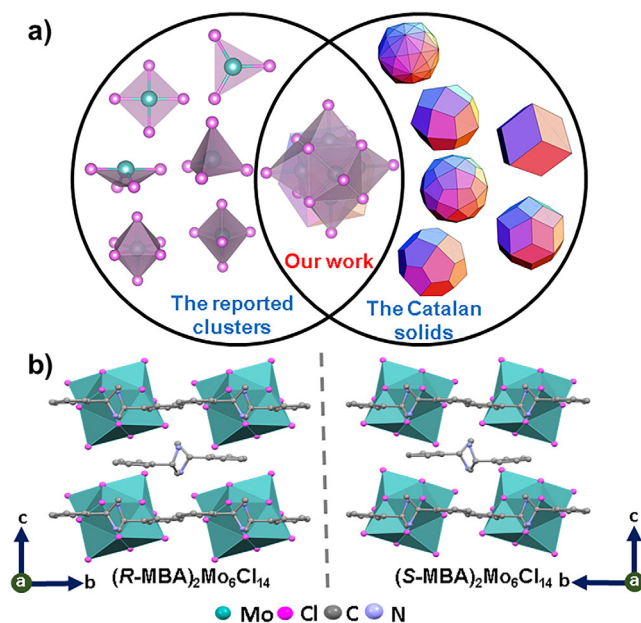


Figure 1. a) The depiction of the previously reported chiral metal-halide clusters and the resemblance of our designed system with the tetrakis hexahedron among the Catalan solids. b) Packing diagram of $(R\text{-MBA})_2\text{Mo}_6\text{Cl}_{14}$ and $(S\text{-MBA})_2\text{Mo}_6\text{Cl}_{14}$ tetrakis hexahedra. Mo, Cl, C, and N are represented by green, magenta, light grey, and light blue spheres, respectively. All hydrogen atoms are omitted for clarity.

to the lattice expansion with the increment in the measuring temperature (represented in Figure S3a,b).^[41]

The $\text{Mo}_6\text{Cl}_{14}^{2-}$ tetrakis hexahedron was unfolded along the Mo–Mo and Cl–Cl bond directions, and the corresponding geometric parameters are shown in Figure 2a (also in Figure S4a,b). Both the Mo–Cl and Mo–Mo bond lengths exhibit irregularities, which are assigned to the distortions in the inorganic framework caused by the chiral organic cations. To quantify this bond length distortion, the bond length distortion index (D) is calculated based on Equation 1,^[42–44]

$$D = \frac{1}{n} \sum_{i=1}^n \frac{|d_i - d_0|}{d_0} \quad (1)$$

where d_i represents the Mo–Mo or Mo–Cl bond length, d_0 is the average Mo–Mo or Mo–Cl bond length, and n denotes the number of such bonds. As shown in Table S2, the calculated D for the Mo–Mo bond is 0.00073, and 0.00126 for the Mo–Cl bond in $(R\text{-MBA})_2\text{Mo}_6\text{Cl}_{14}$ tetrakis hexahedron. Meanwhile, for $(S\text{-MBA})_2\text{Mo}_6\text{Cl}_{14}$ tetrakis hexahedron, the calculated D for Mo–Mo and Mo–Cl bonds is 0.00063 and 0.00148, respectively. As a comparison, the calculated D for Mo–Mo and Mo–Br bonds in achiral $\text{Mo}_6\text{Br}_8(\text{CF}_3\text{COO})_6$ is only 0.00035 and 0.00113,^[45] which is significantly smaller than that of $(R\text{-MBA})_2\text{Mo}_6\text{Cl}_{14}$ and $(S\text{-MBA})_2\text{Mo}_6\text{Cl}_{14}$ tetrakis hexahedra.

To further quantify the distortion degree, the distortion index (σ) of the bond angle is also calculated by using

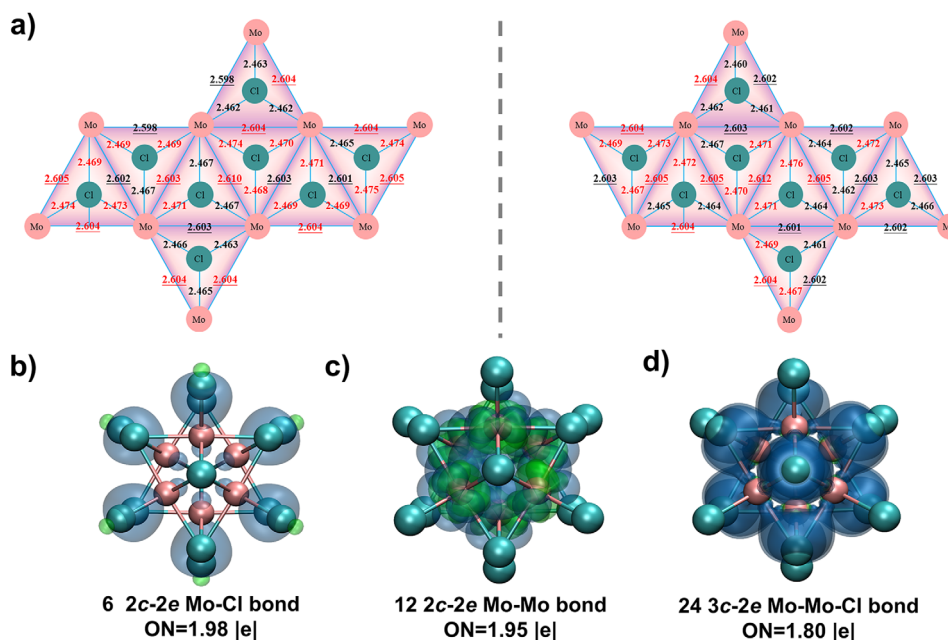


Figure 2. Bonding analysis in the $(R\text{-MBA})_2\text{Mo}_6\text{Cl}_{14}$ and $(S\text{-MBA})_2\text{Mo}_6\text{Cl}_{14}$ tetrakis hexahedra. a) With specific bond lengths and crystal clusters expanded along the Mo–Mo bond direction, red signifies that the bond length is longer than the average value of this type of bond, while black represents bond length shorter than the average. b)–d) AdNDP orbitals of $\text{Mo}_6\text{Cl}_{14}^{2-}$ tetrakis hexahedra. ON represents the occupancy number.

Equation 2,^[13]

$$\sigma = \frac{1}{n} \sum_{i=1}^n \frac{|\theta_i - 90^\circ|}{90^\circ} \quad (2)$$

where θ_i depicts the Cl–Mo–Cl bond angle in the $\text{Mo}_6\text{Cl}_{14}^{2-}$ tetrakis hexahedron. The calculated σ is 0.01342, and 0.01349 for $(R\text{-MBA})_2\text{Mo}_6\text{Cl}_{14}$ and $(S\text{-MBA})_2\text{Mo}_6\text{Cl}_{14}$, respectively. Compared with the previously reported achiral Mo clusters, our designed chiral clusters exhibit significantly larger bond and angle distortions,^[46] providing further evidence that chirality is successfully transferred to the inorganic clusters by the chiral organic cations.

In addition, to further analyze the bonding order within the $\text{Mo}_6\text{Cl}_{14}^{2-}$ tetrakis hexahedron, the adaptive natural density partitioning (AdNDP) wave function analysis was performed. As shown in Figure 2b–d, the $\text{Mo}_6\text{Cl}_{14}^{2-}$ tetrakis hexahedron exhibits three distinct bonding modes. The first mode consists of six 2c-2e Mo–Cl bonds, representing the typical covalent interactions between Mo and Cl atoms. The second mode involves 12 2c-2e Mo–Mo bonds, indicating direct metal–metal interactions. The third, more unique mode, is the 3c-2e Mo–Mo–Cl bond, where a single chloride ion bridges two Mo atoms, resulting in a total of 24 such multicentered bonds. These 3c-2e Mo–Mo–Cl bonds enhance the structural stability and connectivity of the cluster's framework. The interplay of these bonding modes, especially the multicenter bonds, suggests that these clusters may exhibit distinctive electronic properties, such as delocalized electron density and enhanced stability, making them promising candidates for various technological applications.

The electronic and chiroptical properties of the $(R\text{-MBA})_2\text{Mo}_6\text{Cl}_{14}$ and $(S\text{-MBA})_2\text{Mo}_6\text{Cl}_{14}$ were then investigated and shown in Figure 3. The UV–vis spectra for the designed $(R\text{-MBA})_2\text{Mo}_6\text{Cl}_{14}$ and $(S\text{-MBA})_2\text{Mo}_6\text{Cl}_{14}$ chiral tetrakis hexahedron were measured (as shown in Figure 3a). The absorption spectra for the chiral cations ($R\text{-MBACl}$ and $S\text{-MBACl}$) show the excitonic peak ranging from 254 to 270 nm,^[29] while the designed chiral tetrakis hexahedra have similar absorption spectra for both the enantiomers ranging from 250 to 700 nm. It is considered that the absorption spectra for the $(R\text{-MBA})_2\text{Mo}_6\text{Cl}_{14}$ and $(S\text{-MBA})_2\text{Mo}_6\text{Cl}_{14}$ originated from the metal–metal charge transfer (MMCT).^[47,48] The CD spectra display mirror-symmetric signals from 250 to 700 nm for $(R\text{-MBA})_2\text{Mo}_6\text{Cl}_{14}$ and $(S\text{-MBA})_2\text{Mo}_6\text{Cl}_{14}$. Compared with the CD spectra of the chiral cations ($R\text{-MBACl}$ and $S\text{-MBACl}$),^[29] it is confirmed that the chirality is successfully transferred from the chiral organic cations to the inorganic cluster, as shown in Figure 3b.

To further elucidate the optical properties of these clusters, the electronic band structure and projected density of states (PDOS) of $(R\text{-MBA})_2\text{Mo}_6\text{Cl}_{14}$ were also calculated based on the density functional theory (DFT, as shown in Figures 3c and S5). The flat band is consistent with the 0D structural features. The valence band maximum (VBM) and conduction band minimum (CBM) are primarily contributed by the Mo atoms. The isosurface plots of the wave functions for the VBM and CBM further demonstrate that the electron density is predominantly localized on the Mo cluster, as illustrated in Figure 3d.

The room temperature photoluminescence spectra of both $(R\text{-MBA})_2\text{Mo}_6\text{Cl}_{14}$ and $(S\text{-MBA})_2\text{Mo}_6\text{Cl}_{14}$ tetrakis hexahedra were then measured under the 375 nm excitation, and two distinct emission bands at 658 and 698 nm were

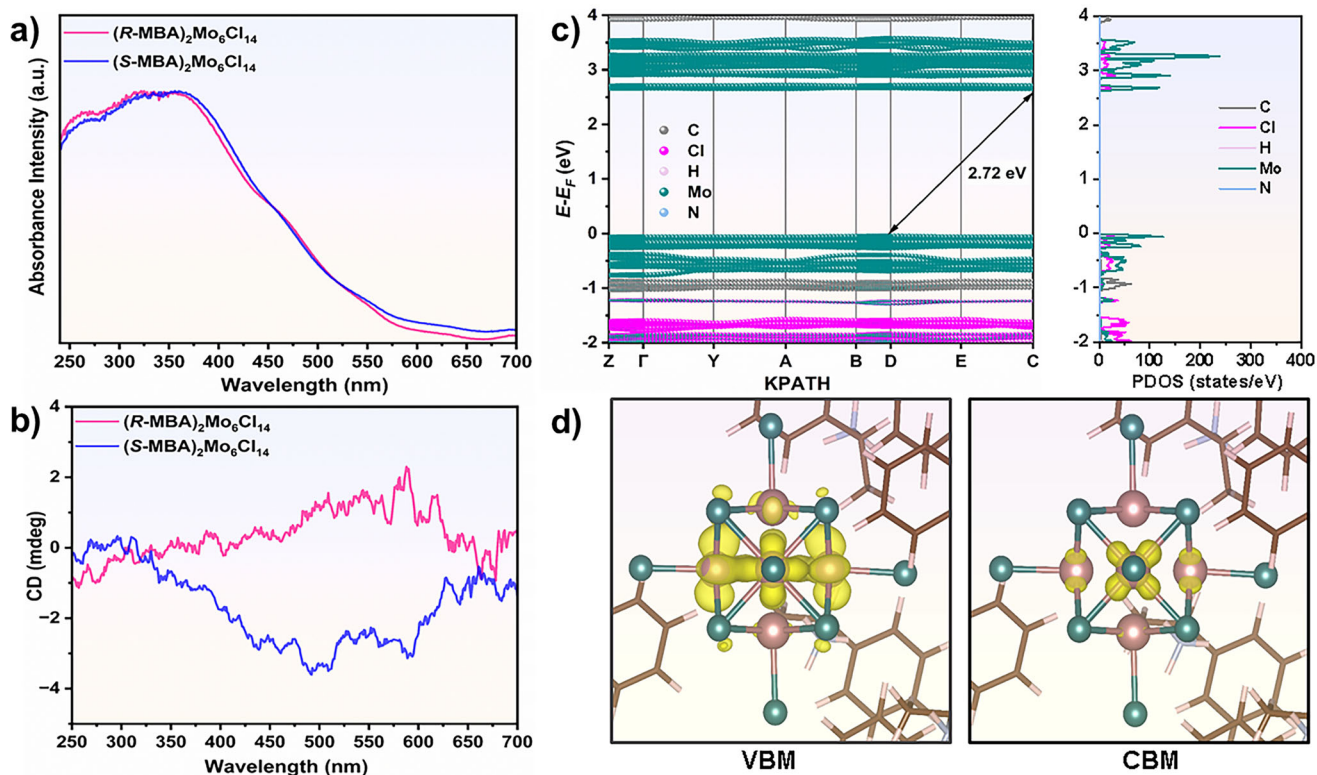


Figure 3. Electronic and chiroptical properties of $(R\text{-MBA})_2\text{Mo}_6\text{Cl}_{14}$ and $(S\text{-MBA})_2\text{Mo}_6\text{Cl}_{14}$ tetrakis hexahedra. a) The absorption spectra of $(R\text{-MBA})_2\text{Mo}_6\text{Cl}_{14}$ and $(S\text{-MBA})_2\text{Mo}_6\text{Cl}_{14}$ tetrakis hexahedra. b) The CD spectra of $(R\text{-MBA})_2\text{Mo}_6\text{Cl}_{14}$ and $(S\text{-MBA})_2\text{Mo}_6\text{Cl}_{14}$ tetrakis hexahedra. c) The band structure and PDOS of $(R\text{-MBA})_2\text{Mo}_6\text{Cl}_{14}$ tetrakis hexahedron. d) The isosurface plots of the VBM and CBM wave functions of $(R\text{-MBA})_2\text{Mo}_6\text{Cl}_{14}$ tetrakis hexahedron.

observed (as shown in Figure 4a). The emission spectra of $(R\text{-MBA})_2\text{Mo}_6\text{Cl}_{14}$ and $(S\text{-MBA})_2\text{Mo}_6\text{Cl}_{14}$ tetrakis hexahedra after 3 months of storage were also measured and shown in Figure S6a,b, which confirms the excellent optical stability of these chiral molybdenum halide tetrakis hexahedra. The dual-band emission peak originated from the different states. It is considered that the high-energy peak originates from bright excitons, while the low-energy band is a convolution of triplet-bright and singlet-dark excitons.^[49] The detailed emission mechanism has been explained in the lateral part by using four-state spin sublevel model. The Commission International de l'Éclairage (CIE) coordinates of $(R/S\text{-MBA})_2\text{Mo}_6\text{Cl}_{14}$ are 0.63 and 0.35 (as shown in Figure 4b), which closely match the standard red emission coordinates (0.67 and 0.33) in the National Television Standard Committee (NTSC).^[50] The photographs of $(R\text{-MBA})_2\text{Mo}_6\text{Cl}_{14}$ and $(S\text{-MBA})_2\text{Mo}_6\text{Cl}_{14}$ crystals under daylight and UV light are also shown in Figure S7. Therefore, such high color purity of $(R\text{-MBA})_2\text{Mo}_6\text{Cl}_{14}$ and $(S\text{-MBA})_2\text{Mo}_6\text{Cl}_{14}$ makes them promising candidates as pure deep-red CPL emitters.

In addition, the emission wavelengths of these chiral molybdenum halide clusters were also compared with the other previously reported chiral metal halides (as depicted in Figure S8), illustrating that the emission of our chiral tetrakis hexahedra covers a wider range of the visible spectrum.^[22,23,26,51] The PLQY of $(R\text{-MBA})_2\text{Mo}_6\text{Cl}_{14}$ and $(S\text{-MBA})_2\text{Mo}_6\text{Cl}_{14}$ is 7.58% and 7.41%, respectively, as shown

in Figure S9. We also compared the PLOQY of the previously reported achiral molybdenum compounds with our chiral cluster, and a significantly increased PLOQY is observed (as shown in Figure S10).^[52]

To further investigate the chiroptical properties of the $(R\text{-MBA})_2\text{Mo}_6\text{Cl}_{14}$ and $(S\text{-MBA})_2\text{Mo}_6\text{Cl}_{14}$ tetrakis hexahedra, their CPL spectra were measured and shown in Figure 4c. The mirror-symmetric CPL spectra of $(R\text{-MBA})_2\text{Mo}_6\text{Cl}_{14}$ and $(S\text{-MBA})_2\text{Mo}_6\text{Cl}_{14}$ range from 650 to 700 nm were observed, confirming that they are promising candidates as pure deep-red CPL emitters. The CPL peaks are consistent with the PL spectra as discussed above, providing further evidence of successful chirality transfer from chiral cations to the molybdenum halide. The luminescence dissymmetry factor (g_{lum}) of the CPL was then calculated by using Equation 3,^[53–56]

$$g_{\text{lum}} = 2 \frac{I_L - I_R}{I_L + I_R} \quad (3)$$

where I_L and I_R depict the intensities of the left- and right-handed CPL, respectively. The g_{lum} evaluated for $(R\text{-MBA})_2\text{Mo}_6\text{Cl}_{14}$ and $(S\text{-MBA})_2\text{Mo}_6\text{Cl}_{14}$ at 658 nm are 6.07×10^{-4} and -5.64×10^{-4} , while at 698 nm are -6.30×10^{-4} and 9.10×10^{-4} , respectively, as shown in Figure S11.

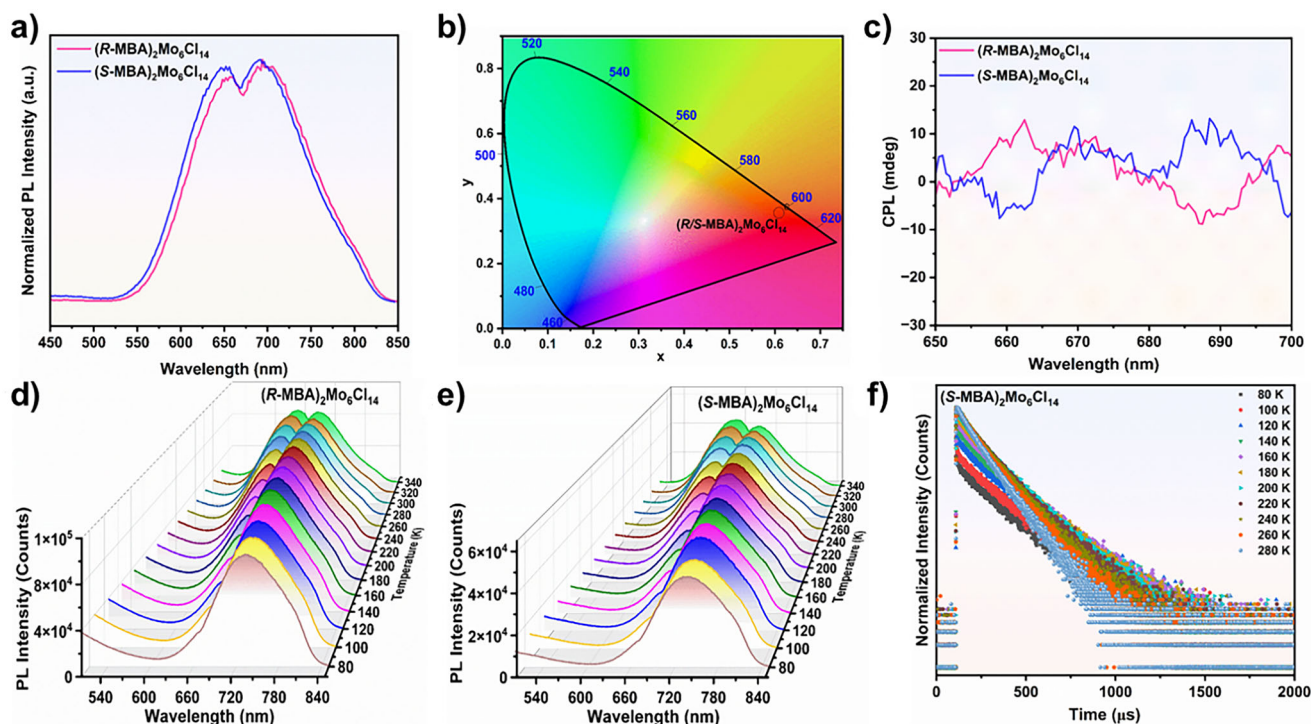


Figure 4. Luminescent properties of $(R\text{-MBA})_2\text{Mo}_6\text{Cl}_{14}$ and $(S\text{-MBA})_2\text{Mo}_6\text{Cl}_{14}$ tetrakis hexahedra. a) The PL spectra of $(R\text{-MBA})_2\text{Mo}_6\text{Cl}_{14}$ and $(S\text{-MBA})_2\text{Mo}_6\text{Cl}_{14}$ tetrakis hexahedra excited at 375 nm. b) The CIE spectra of $(R\text{-MBA})_2\text{Mo}_6\text{Cl}_{14}$ and $(S\text{-MBA})_2\text{Mo}_6\text{Cl}_{14}$ tetrakis hexahedra. c) The CPL spectra of $(R\text{-MBA})_2\text{Mo}_6\text{Cl}_{14}$ and $(S\text{-MBA})_2\text{Mo}_6\text{Cl}_{14}$ tetrakis hexahedra. d) The temperature-dependent emission spectra of $(R\text{-MBA})_2\text{Mo}_6\text{Cl}_{14}$ tetrakis hexahedron excited at 375 nm. e) The temperature-dependent emission spectra of $(S\text{-MBA})_2\text{Mo}_6\text{Cl}_{14}$ tetrakis hexahedron excited at 375 nm. f) The temperature-dependent lifetime spectra of $(S\text{-MBA})_2\text{Mo}_6\text{Cl}_{14}$ tetrakis hexahedron.

To gain a deeper understanding of the emission mechanism in $(R\text{-MBA})_2\text{Mo}_6\text{Cl}_{14}$ and $(S\text{-MBA})_2\text{Mo}_6\text{Cl}_{14}$ tetrakis hexahedra, temperature-dependent PL spectra were measured over a range from 80 to 340 K and presented in Figure 4d,e. A strong correlation between the broadness of the emission peak and temperature is observed, which indicates enhanced optical phonon scattering with increasing temperature. As the temperature increases, a weak peak at approximately 658 nm becomes prominent at 160 K, representing the redshift from the existing peak around 700 nm. The monotonic decrease in the emission intensity with the temperature increases from 80 to 340 K. This behavior should be attributed to the suppression of nonradiative decay due to thermally populated vibrational states, as discussed in the subsequent section.^[57,58]

To further explore the photophysical dynamics of these chiral molybdenum halide clusters, the temperature-dependent lifetime of $(S\text{-MBA})_2\text{Mo}_6\text{Cl}_{14}$ was measured across the 80–280 K range, as shown in Figure 4f. The average PL lifetime (τ_{av}) is well-fitted with a bi-exponential function based on Equation 4,^[59,60]

$$\tau_{\text{av}} = \frac{\sum_{i=1}^n \alpha_i \tau_i^2}{\alpha_i \tau_i} \quad (4)$$

here, τ_i represents the decay time of the i_{th} component, and α_i represents the amplitude of the i_{th} component. The PL lifetimes for $(R\text{-MBA})_2\text{Mo}_6\text{Cl}_{14}$ and $(S\text{-MBA})_2\text{Mo}_6\text{Cl}_{14}$

at room temperature are 113.83 and 113.87 μs at 658 nm and 114.14 and 113.77 μs at 698 nm, respectively, as shown in Figure S12. This prolonged lifetime is attributed to electron-phonon coupling, which enhances defect tolerance and stability by suppressing carrier recombination.^[61]

The radiative (k_r) and nonradiative decay constants (k_{nr}) of $(R\text{-MBA})_2\text{Mo}_6\text{Cl}_{14}$ and $(S\text{-MBA})_2\text{Mo}_6\text{Cl}_{14}$ tetrakis hexahedra are then calculated based on PLQY and PL lifetime (as summarized in Tables S3 and S4). The calculated k_r at 658 nm is 6.66×10^2 and $6.51 \times 10^2 \text{ s}^{-1}$ for $(R\text{-MBA})_2\text{Mo}_6\text{Cl}_{14}$ and $(S\text{-MBA})_2\text{Mo}_6\text{Cl}_{14}$, respectively, while k_{nr} is 8.12×10^3 and $8.13 \times 10^3 \text{ s}^{-1}$, respectively. Similarly, the calculated k_r at 698 nm is 6.64×10^2 and $6.51 \times 10^2 \text{ s}^{-1}$, while k_{nr} is 8.10×10^3 and $8.14 \times 10^3 \text{ s}^{-1}$ for $(R\text{-MBA})_2\text{Mo}_6\text{Cl}_{14}$ and $(S\text{-MBA})_2\text{Mo}_6\text{Cl}_{14}$, respectively. These decay constants are comparable to the previously reported Mo halide clusters. The smaller k_r should be due to the symmetric and spin-forbidden radiative transition from the excited state to the ground state,^[62,63] while the reduced k_{nr} values reflect the increased structural rigidity of our clusters and thus contribute to an improvement in PLQY.^[64]

The averaged PL lifetime ($\tau(T)$) of $(S\text{-MBA})_2\text{Mo}_6\text{Cl}_{14}$ from 80 to 280 K was then systematically investigated, which exhibits an inverse relationship with the temperature, as illustrated in Figures 4f, S13, S14, and Table S5. To gain deeper insight into the emission mechanism, an excited four-state spin sublevel model (Φ_n , $n = 1, 2, 3, 4$) was employed. In this model, the singlet exciton (S_1) undergoes the fast

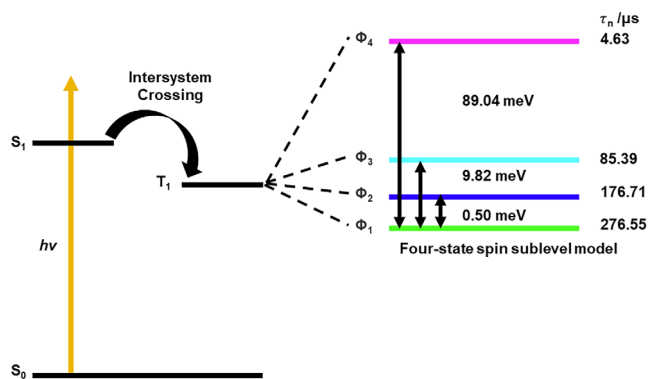


Figure 5. The emission mechanism by employing a four-state spin sublevel model.

intersystem crossing (ISC) to the triplet (T_1) state owing to the strong spin-orbit coupling (SOC) of molybdenum. During this process, the change in spin momentum (i.e., the change in spin quantum number, n) is compensated by a corresponding change in the angular momentum (i.e., a change in the azimuthal quantum number, $l > 1$). Then the degenerated T_1 state of $(R\text{-MBA})_2\text{Mo}_6\text{Cl}_{14}$ and $(S\text{-MBA})_2\text{Mo}_6\text{Cl}_{14}$ will be split into four spin sublevels (Φ_n) due to the generation of zero-magnetic field (ZFS). The excited state behavior of our system was further analyzed by using Equation 5.^[65]

$$\tau(T) = \frac{\sum g_n \exp(-\Delta E_{1n}/k_B T)}{\sum \frac{g_n}{\tau_n} \exp(-\Delta E_{1n}/k_B T)} \quad (5)$$

where g_n ($n = 1, 2, 3, 4$; $g_1 = g_3 = 2$, $g_2 = 1$, and $g_4 = 3$), represents the multiplicity of the different states in the designed system serving as the statistical weight in the equation, and τ_n is the emission lifetime of Φ_n , respectively. The analysis of the $\tau(T)$ was carried out by using τ_n ($n = 1-4$) and the zero-field splitting energy between Φ_1 and Φ_n ($n = 2-4$, ΔE_{1n}) as the fitting parameters. The ΔE_{12} is fixed to 0.50 meV for the simulations, as the splitting between Φ_1 and Φ_2 is attributed to the Jahn–Teller distortion.

The fitting results for the four-state spin sublevels (Φ_n , $n = 1-4$) are given in Figure 5. The four-state spin sublevel model focuses specifically on spin-dependent transitions within the Mo cluster (not the MBA ligand). The S_0 and S_1 represent the spin sublevels of the Mo cluster's excited-state manifold, consistent with the electronic structural analysis in Figure 3c,d. The chiral ligand does not directly participate in the spin sublevel transitions modeled here. These results reveal that the two emission bands originate from relaxations of different excited states. At lower temperatures, electrons lack sufficient kinetic energy to overcome the potential barrier. As the temperature increases, electrons accumulate larger kinetic energy, enhancing the possibility of crossing the barrier. Consequently, the population of electrons in lower-energy states decreases. In contrast, electrons in higher-energy states become more populated at room temperature, leading to the observed dual-band emission in the designed tetrakis hexahedra.^[66,67]

Conclusion

In summary, the first chiral molybdenum halide, $(R\text{-MBA})_2\text{Mo}_6\text{Cl}_{14}$ and $(S\text{-MBA})_2\text{Mo}_6\text{Cl}_{14}$ tetrakis hexahedra, were synthesized to construct the deep-red CPL emitters. The combination of the unique optical properties of molybdenum halide with chirality produces the mirror-symmetric tetrakis hexahedra structures in $(R\text{-MBA})_2\text{Mo}_6\text{Cl}_{14}$ and $(S\text{-MBA})_2\text{Mo}_6\text{Cl}_{14}$. These chiral molybdenum halide clusters exhibit the 24 unique $3c-2e$ Mo–Mo–Cl bond (the so-called multicenter bonds), which are rarely reported in traditional chiral metal halides. The chiroptical properties of $(R\text{-MBA})_2\text{Mo}_6\text{Cl}_{14}$ and $(S\text{-MBA})_2\text{Mo}_6\text{Cl}_{14}$ tetrakis hexahedra, including CD and CPL, were thoroughly investigated, and it was found that they exhibit efficient deep-red CPL emission, extended lifetimes, enhanced optical stability, and improved PLQY compared to their achiral counterparts. The four-state spin sublevel model reveals that the dual-band emission arises from the temperature-dependent exciton dynamics. Our findings expand the family of lead-free chiral metal halides and offer valuable insights into the development of novel chiral lead-free metal halides with efficient deep-red CPL emission.

Acknowledgements

The authors gratefully acknowledge the financial support from the National Natural Science Foundation of China (52473305, 92256202, U22A20399, and 12261131500), the Fundamental Research Funds for the Central Universities, Nankai University (grant number: 023-63233038), the 111 Project (B18030), and the Supercomputing Center of Lanzhou University.

Conflict of Interests

The authors declare no conflict of interest.

Data Availability Statement

The accession numbers for the $(R\text{-MBA})_2\text{Mo}_6\text{Cl}_{14}$ and $(S\text{-MBA})_2\text{Mo}_6\text{Cl}_{14}$ tetrakis hexahedron crystal structure CIFs reported in this paper are CCDC: 2370510 and 237051, respectively. The crystallographic data for $(R\text{-MBA})_2\text{Mo}_6\text{Cl}_{14}$ and $(S\text{-MBA})_2\text{Mo}_6\text{Cl}_{14}$ in this paper can be obtained free of charge from <https://www.ccdc.cam.ac.uk/>.

Keywords: Catalan solid • Chiral metal halide • Circularly polarized luminescence • Deep-red emission • Tetrakis hexahedra

[1] M. Zhang, Q. Guo, Z. Li, Y. Zhou, S. Zhao, Z. Tong, Y. Wang, G. Li, S. Jin, M. Zhu, T. Zhuang, S. H. Yu, *Sci. Adv.* **2023**, 9, eadi9944.

- [2] Z. Yang, H. Lu, Y. Zhang, B. Yin, H. Wang, S. Gull, W. Qin, Y. Chen, J. Yao, C. Zhang, G. Long, *Laser Photonics Rev.* **2024**, *18*, 2400040.
- [3] S. Lin, Y. Tang, W. Kang, H. K. Bisoyi, J. Guo, Q. Li, *Nat. Commun.* **2023**, *14*, 3005.
- [4] Y. Dang, X. Liu, B. Cao, X. Tao, *Matter*, **2021**, *4*, 794–820.
- [5] Y. Zhang, S. Yu, B. Han, Y. Zhou, X. Zhang, X. Gao, Z. Tang, *Matter* **2022**, *5*, 837–875.
- [6] M. Li, Y. Wang, L. Yang, Z. Chai, Y. Wang, S. Wang, *Angew. Chem. Int. Ed.* **2022**, *61*, e202208440.
- [7] J. Ma, C. Fang, C. Chen, L. Jin, J. Wang, S. Wang, J. Tang, D. Li, *ACS Nano* **2019**, *13*, 3659–3665.
- [8] M. Khorloo, X. Yu, Y. Cheng, H. Zhang, S. Yu, J. W. Y. Lam, M. Zhu, B. Z. Tang, *ACS Nano* **2021**, *15*, 1397–1406.
- [9] X. Yu, S. Zhong, Z. Guo, J. Guan, H. Tang, X. He, Y. Chen, S. Pan, *J. Mater. Chem. C* **2025**, *13*, 2190–2197.
- [10] C. Zhang, S. Li, X. Y. Dong, S. Q. Zang, *Aggregate* **2021**, *2*, e48.
- [11] Q. Wang, H. Zhu, Y. Tan, J. Hao, T. Ye, H. Tang, Z. Wang, J. Ma, J. Sun, T. Zhang, F. Zheng, W. Zhang, H. W. Choi, W. C. H. Choy, D. Wu, X. W. Sun, K. Wang, *Adv. Mater.* **2024**, *36*, 2305604.
- [12] H. Wang, J. Li, H. Lu, S. Gull, T. Shao, Y. Zhang, T. He, Y. Chen, T. He, G. Long, *Angew. Chem. Int. Ed.* **2023**, *62*, e202309600.
- [13] H. Lu, T. He, H. Wu, F. Qi, H. Wang, B. Sun, T. Shao, T. Qiao, H. L. Zhang, D. Sun, Y. Chen, Z. Tang, G. Long, *Adv. Funct. Mater.* **2024**, *34*, 2308862.
- [14] X. Fu, Z. Zeng, S. Jiao, X. Wang, J. Wang, Y. Jiang, W. Zheng, D. Zhang, Z. Tian, Q. Li, A. Pan, *Nano Lett.* **2023**, *23*, 606–613.
- [15] H. Duim, M. A. Loi, *Matter* **2021**, *4*, 3835–3851.
- [16] J. Bai, H. Wang, J. Ma, Y. Zhao, H. Lu, Y. Zhang, S. Gull, T. Qiao, W. Qin, Y. Chen, L. Jiang, G. Long, Y. Wu, *J. Am. Chem. Soc.* **2024**, *146*, 18771–18780.
- [17] K. Wei, B. Liang, C. Sun, Y. Jiang, M. Yuan, *Small Struct.* **2022**, *3*, 2200063.
- [18] X. Tian, K. Shoyama, B. Mahlmeister, F. Brust, M. Stolte, F. Wuerthner, *J. Am. Chem. Soc.* **2023**, *145*, 9886–9894.
- [19] M. Tsuji, S. Abuhadba, A. Chen, M. Ito, A. Makhijani, Y. Kuwahara, T. Espipova, T. Mani, *J. Phys. Chem. B* **2023**, *127*, 9781–9787.
- [20] G. F. Huo, W. T. Xu, J. Hu, Y. Han, W. Fan, W. Wang, Z. Sun, H. B. Yang, J. Wu, *Angew. Chem. Int. Ed.* **2024**, *64*, e202416707.
- [21] E. E. Morgan, A. Brumberg, S. Panuganti, G. T. Kent, A. Zohar, A. A. Mikhailovsky, M. G. Kanatzidis, R. D. Schaller, M. L. Chabiny, A. K. Cheetham, R. Seshadri, *Chem. Mater.* **2024**, *36*, 7754–7763.
- [22] J. Chen, S. Zhang, X. Pan, R. Li, S. Ye, A. K. Cheetham, L. Mao, *Angew. Chem. Int. Ed.* **2022**, *61*, e202205906.
- [23] M. Wang, X. Wang, B. Zhang, F. Li, H. Meng, S. Liu, Q. Zhao, *J. Mater. Chem. C* **2023**, *11*, 3206–3212.
- [24] H. Lu, F. Qi, H. Wang, T. He, B. Sun, X. Gao, A. H. Comstock, S. Gull, Y. Zhang, T. Qiao, T. Shao, Y. X. Zheng, D. Sun, Y. Chen, H. L. Zhang, Z. Tang, G. Long, *Angew. Chem. Int. Ed.* **2025**, *64*, e202415363.
- [25] Y. Deng, F. Li, Z. Zhou, M. Wang, Y. Zhu, J. Zhao, S. Liu, Q. Zhao, *Chin. Chem Lett.* **2024**, *35*, 109085.
- [26] J. Guan, Y. Zheng, P. Cheng, W. Han, X. Han, P. Wang, M. Xin, R. Shi, J. Xu, X. H. Bu, *J. Am. Chem. Soc.* **2023**, *145*, 26833–26842.
- [27] C. F. Wang, C. Shi, A. Zheng, Y. Wu, L. Ye, N. Wang, H. Y. Ye, M. G. Ju, P. Duan, J. Wang, Y. Zhang, *Mater. Horiz.* **2022**, *9*, 2450–2459.
- [28] J. Ren, T. He, H. Lu, H. Wang, T. Shao, Z. Wang, Y. Zhang, S. Gull, Y. Chi, Y. W. Zhong, Y. Chen, G. Long, *Mater. Horiz.* **2024**, *11*, 6089–6097.
- [29] X. Niu, Z. Zeng, Z. Wang, H. Lu, B. Sun, H. L. Zhang, Y. Chen, Y. Du, G. Long, *Sci. China Chem.* **2024**, *67*, 1961–1968.
- [30] L. He, P. P. Shi, L. Zhou, Z. B. Liu, W. Zhang, Q. Ye, *Chem. Mater.* **2021**, *33*, 6233–6239.
- [31] U. Palmqvist, P. Leisner, E. Ahlberg, *J. Electrochem. Soc.* **2024**, *171*, 042501.
- [32] L. Li, X. Liu, G. Liu, S. Xu, G. Hu, L. Wang, *Nat. Commun.* **2024**, *15*, 8720.
- [33] K. Kirakci, J. Zelenka, I. Krizova, T. Ruml, K. Lang, *Inorg. Chem.* **2020**, *59*, 9287–9293.
- [34] W. Hua, H. H. Sun, F. Xu, J. G. Wang, *Rare Met.* **2020**, *39*, 335–351.
- [35] Y. A. Vorotnikov, O. A. Efremova, I. N. Novozhilov, V. V. Yanshole, N. V. Kuratieva, K. A. Brylev, N. Kitamura, Y. V. Mironov, M. A. Shestopalov, *J. Mol. Struct.* **2017**, *1134*, 237–243.
- [36] Y. Wei, V. Veryazov, L. Kantorovich, *APL Mater.* **2024**, *12*, 01127.
- [37] *Dual Models* (Ed: M. J. Wenninger), Cambridge University Press, Cambridge **1983**, pp. 14–35.
- [38] M. Koca, N. Ozdes Koca, R. Koc, *J. Math. Phys.* **2010**, *51*, 043501.
- [39] J. Batle, A. V. Shutov, A. V. Maleev, *Phys. Lett. A* **2020**, *384*, 126919.
- [40] O. Gelisgen, Z. Colak, *ACAM* **2015**, *24*, 3–15.
- [41] J. Zhao, X. Liu, Z. Wu, B. Ibrahim, J. Thieme, G. Brocks, S. Tao, L. J. Bannenberg, T. J. Savenije, *Adv. Funct. Mater.* **2024**, *34*, 2311727.
- [42] Z. Wang, X. Qiu, H. Wang, W. Zhao, S. Gull, H. Lu, Z. Hao, B. Sun, X. Zeng, X. Liu, H. L. Zhang, Y. Chen, T. He, G. Long, *Angew. Chem. Int. Ed.* **2025**, *64*, e202420249.
- [43] T. Song, C. Q. Wang, H. Lu, X. J. Mu, B. L. Wang, J. Z. Liu, B. Ma, J. Cao, C. X. Sheng, G. Long, Q. Wang, H. L. Zhang, *Angew. Chem. Int. Ed.* **2024**, *63*, e202400769.
- [44] Q. Guan, H. Ye, T. Zhu, X. Zhang, S. You, J. Wu, Y. Zheng, X. Liu, J. Luo, *Adv. Opt. Mater.* **2023**, *11*, 2202726.
- [45] K. Kirakci, P. Kubát, J. Langmaier, T. Polívka, M. Fuciman, K. Fejfarová, K. Lang, *Dalton Trans.* **2013**, *42*, 7224–7232.
- [46] N. Prokopuk, D. F. Shriver, *Inorg. Chem.* **1997**, *36*, 5609–5613.
- [47] X. Zarate, E. Schott, L. A. Soto, R. R. Tagle, *Chem. Phys. Lett.* **2013**, *567*, 39–42.
- [48] R. R. Tagle, R. A. Perez, *Chem. Phys. Lett.* **2008**, *460*, 438–441.
- [49] Z. Kuang, X. Huang, X. Wang, C. Wang, X. Wang, W. Huang, Q. Peng, *J. Wang, Natl. Sci. Rev.* **2024**, *12*, nwa180.
- [50] K. Singh, M. Rajendran, R. Devi, S. Vaidyanathan, *Dalton Trans.* **2021**, *50*, 4986–5000.
- [51] J. Lu, B. Shao, R. W. Huang, L. G. Arzaluz, S. Chen, Z. Han, J. Yin, H. Zhu, S. Dayneko, M. N. Hedhili, X. Song, P. Yuan, C. Dong, R. Zhou, M. I. Saidaminov, S. Q. Zang, O. F. Mohammed, O. M. Bakr, *J. Am. Chem. Soc.* **2024**, *146*, 4144–4152.
- [52] Y. Liu, Y. Wei, Z. Luo, B. Xu, M. He, P. Hong, C. Li, Z. Quan, *Chem. Sci.* **2024**, *15*, 15480–15488.
- [53] C. H. Yang, S. B. Xiao, H. Xiao, L. J. Xu, Z. N. Chen, *ACS Nano* **2023**, *17*, 7830–7836.
- [54] Q. Wei, Z. Ning, *ACS Mater. Lett.* **2021**, *3*, 1266–1275.
- [55] S. Ma, J. Ahn, J. Moon, *Adv. Mater.* **2021**, *33*, 2005760.
- [56] H. Lu, Z. V. Vardeny, M. C. Beard, *Nat. Rev. Chem.* **2022**, *6*, 470–485.
- [57] S. Zhou, Y. Chen, K. Li, X. Liu, T. Zhang, W. Shen, M. Li, L. Zhou, R. He, *Chem. Sci.* **2023**, *14*, 5415–5424.
- [58] Z. Li, Y. Li, P. Liang, T. Zhou, L. Wang, R. J. Xie, *Chem. Mater.* **2019**, *31*, 9363–9371.
- [59] *Principles of Fluorescence Spectroscopy* (Ed: J. R. Lakowicz), Springer, Boston, MA **2006**, pp. 97–155.
- [60] W. N. Lee, L. H. Lai, Y. Q. Tu, Y. H. Chang, L. Y. Chen, H. C. Chang, C. C. Hsieh, J. J. Wu, *Mater. Today Phys.* **2024**, *41*, 101339.
- [61] K. Coustas, A. Garreau, A. Buolou, B. Fontaine, J. Cuny, R. Gautier, M. Mortier, Y. Molard, J. L. Duvaill, E. Faulques, S. Cordier, *Phys. Chem. Chem. Phys.* **2015**, *17*, 28574–28585.
- [62] L. Luo, Z. Liu, A. Mazumder, R. Jin, *J. Am. Chem. Soc.* **2024**, *146*, 27993–27997.

- [63] N. Du, S. Yu, Y. Xie, Y. Cui, L. Zhang, M. Yang, *Eur. Phys. J. B* **2019**, *92*, 280.
- [64] Y. Saito, H. K. Tanaka, Y. Sasaki, T. Azumi, *J. Phys. Chem.* **1985**, *89*, 4413–4415.
- [65] S. Akagi, S. Fujii, N. Kitamura, *J. Phys. Chem. A* **2018**, *122*, 9014–9024.
- [66] X. Meng, S. Ji, Q. Wang, X. Wang, T. Bai, R. Zhang, B. Yang, Y. Li, Z. Shao, J. Jiang, K. I. Han, F. Liu, *Adv. Sci.* **2022**, *9*, 2203596.
- [67] J. A. Lai, C. Li, Z. Wang, L. Guo, Y. Wang, K. An, S. Cao, D. Wu, Z. Liu, Z. Hu, Y. Leng, J. Du, P. He, X. Tang, *Chem. Eng. J.* **2024**, *494*, 153077.

Manuscript received: January 24, 2025

Revised manuscript received: May 19, 2025

Accepted manuscript online: June 23, 2025

Version of record online: June 30, 2025